COMPOSITIONAL PROVINCES OF MARS FROM STATISTICAL ANALYSES OF TES, GRS AND CRISM DATA.
A. D. Rogers[1] and V. E. Hamilton[2], [1]Stony Brook University, Stony Brook, NY 11794-2100, Deanne.Rogers@stonybrook.edu, [2]Southwest Research Insitute, Boulder, CO, 80302, hamilton@boulder.swri.edu

Introduction: Global maps of minerals and element concentrations on Mars have been produced using a variety of techniques and spatial scales. These maps reveal compositional associations with terrain age, geologic setting, and surface properties, which have been used to infer processes and events which produced those compositions [e.g., 1-9]. To date, however, few studies have focused on spatial variations in lithology or mineral assemblage, which is critical for investigating processes that influenced crustal development and alteration. In this work, we apply standard statistical methods to mineral distributions modeled from Mars Global Surveyor (MGS) Thermal Emission Spectrometer (TES) data, at a spatial resolution of eight pixels per degree (ppd). Through multivariate analysis of mineral abundance, we identify new regions that were unrecognized as distinct in previous studies. Element mass fraction distributions and VNIR-derived mineral characteristics are also derived for each class.

Methods: TES-derived mineral concentrations from [5] were spatially binned at a resolution of 8 ppd. Regions poleward of +/- 60° latitude were excluded due to low surface temperatures which result in inadequate signal-to-noise ratios. Bins associated with low spectral contrast were also excluded from analysis, due to non-linear mixing of surface components that occurs with small particle sizes (e.g. [10]). The criterion used for bin exclusion was the total modeled contribution of surface components to each TES spectrum, such that any bins with total surface concentrations < 50% were discarded. This resulted in a total of 308,087 bins out of >2.7M bins for analysis.

Independent component analysis (ICA) [11] was used to find the most significant variations in the multivariate data as well as to find small-scale, unique regions of interest (**Fig. 1**). Unlike principal component analysis (PCA), successful ICA assumes the independent physical sources have non-Gaussian distributions. Because some mineral abundances are commonly zero, many of the sources are non-Gaussian in nature. Furthermore, because some compositionally distinct regions comprise a small fraction of the pixels used in the analysis, these small but mineralogically distinct regions could be buried in the lower PC bands despite being a real surface difference. To reduce the dimensionality of the ICA output, bands were sorted by a 2-D spatial coherence value calculated for each band and the lower 12 bands (out of 30) were discarded.

To produce a single map highlighting major compositional provinces and boundaries, pixels were classified using a maximum likelihood classification on the retained ICA bands. Using results from analysis of the ICA bands, 16 polygonal regions of interest (ROIs) were defined for input into the classification. Only pixels with greater than 90% probability for a given class were classified. Any resulting class means with <10% total difference in absolute mineral abundance were then merged. The choice of supervised over unsupervised methods was driven by the need to assign higher significance to spatial coherence than to spatially uncorrelated clusters in the data set.

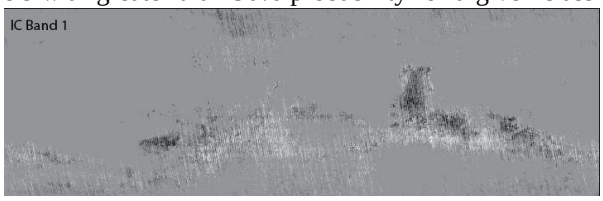

Fig. 1. Example from IC analysis on TES mineral distributions. The first ICA band, using spatial coherence criterion, is shown.

Mars Odyssey Gamma Ray Spectrometer (GRS) element mass fraction maps (H, Th, K, Fe, Si, and Cl, resolution=5° per pixel) and CRISM olivine, low-Ca pyroxene (LCP), and high-Ca pyroxene (HCP) parameter maps (from MSP map tile products, degraded to 8ppd) were first masked using the same mask applied to the TES data (**Fig. 2**). To compare the TES-derived classes with the lower resolution GRS data set, element mass fractions were selected for each pixel in each TES-derived compositional class, as well as for a random population of pixels that was the same size as each TES class, and plotted as histograms with 20 bins per population (**Fig. 3**). Comparison of the TES class and random GRS element characteristics provides a comparison of each class to the global (but masked) data set, using populations of identical size. For the degraded CRISM parameter maps, a nonparametric test of statistical significance, the Mann-Whitney test, was then used to determine whether the CRISM parameter distributions within each TES-derived spectral class are statistically distinct.

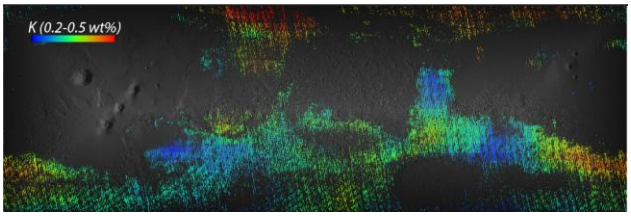

Fig. 2. Example GRS map (K), masked using the same mask applied to the TES data set.

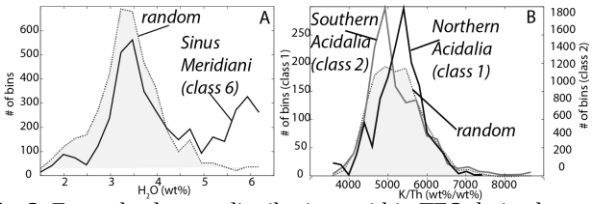

Fig. 3. Example element distributions within TES-derived compositional classes. **A**. H_2O distribution within class 6 is bimodal; higher wt% peak corresponds with areas in Sinus Meridiani. **B**. K/Th distributions within TES classes 1&2 (N. and S. Acidalia).

Major findings include: 1. **Ten mineral assemblage classes were found in Martian low-dust regions** (**Fig. 4,Table 1**). Boundaries observed by [1,4-5] (Syrtis Major, Thaumasia Planum, Acidalia, Meridiani hematite unit, Nili Fossae olivine-bearing unit) are preserved in the new class maps; and new distinctions are apparent.

2. Sinus Meridiani, the low-albedo region bordering the southern margin of the Meridiani Planum hematite unit, is compositionally distinct from similarly-aged heavily cratered terrains. Its class (6) is characterized by higher sulfate and high-Si phase abundance, and lower feldspar abundance than other low-dust surfaces on Mars. Class 6 exhibits a distinctly higher H_2O abundance mode in GRS data (**Fig. 3**), and a moderately higher Fe and Cl abundance, compared to other low-dust regions. Together, the Fe, H_2O and TES sulfate abundances may point to a higher proportion of iron sulfates in the Sinus Meridiani soils. This would be broadly consistent with hydrology models calling for repeated groundwater evaporation in this region [12].

3. **Syrtis Major** may be split into two classes. Areas in north-central and south-central Syrtis Major exhibit higher abundances of HCP relative to areas around the periphery and in the west-central portions of the shield. This new distinction made in the thermal infrared corresponds remarkably well with spectral distinctions made in a recent Syrtis mapping effort by [13] using OMEGA VNIR data. CRISM HCP parameter distributions are also distinct between the two classes at >99% confidence level.

4. Hesperian volcanic provinces in the highlands (Syrtis, Hesperia, and Thaumasia) largely fall into the same TES compositional class (class 8), which is characterized by elevated HCP abundance and lower olivine abundance compared to other highlands classes. Though the areas mapped into Class 8 are mineralogically similar, there is significant geochemical variability within this class. The variations are clustered to specific geographic areas, however. Si is enriched in Thaumasia Planum, but not Syrtis or Hesperia. Th is depleted in Hesperia and Thaumasia Planum, but not Syrtis Major. All three of these regions do exhibit relatively low K concentrations (**Fig 2.**).

5. Northern and southern Acidalia are compositionally distinct. Though it has been noted before by [4, 14], the distinction is so compelling that it bears repeating. Furthermore, this boundary is also evident in K and K/Th maps, with northern Acidalia exhibiting higher K/Th than southern Acidalia (**Fig 3**). The boundary roughly corresponds to a geomorphologic boundary between hummocky terrain and subdued hummocky terrain with polygonally patterned ground [14]. Based on this observation, [14] suggested that the boundary corresponds with the extent of periglacial activity in the north, and that the spectral signatures arise from aqueous weathering in ice-rich soils. Differences in degree of weathering would be consistent with the differences in K/Th observed across this boundary.

Table 1. Class mean mineral abundance and standard deviation (TES-derived)

	Class 1		Class 2		Class 3		Class 4		Class 5		Class 6		Class 7		Class 8		Class 9		Class 10	
	N. Acidalia		S. Acidalia		Central Syrtis		Cratered A		Cratered B		Cratered C		Solis/ Aonium		Thaumasia/ Hesperia/ Syrtis		Meridiani Planum		Nili Fossae	
Feldspar	30	5	27	4	28	3	28	4	29	5	24	4	33	5	28	3	19	3	25	6
Low-Ca pyroxene	21	4	24	4	17	3	21	4	24	5	22	4	20	4	20	4	19	3	18	4
High-Ca pyroxene	3	2	3	2	15	3	10	4	6	3	8	3	4	3	10	3	4	2	9	4
Olivine	1	1	2	2	7	2	9	2	6	3	8	2	3	2	6	2	5	1	12	5
High-Si Phases	27	5	22	4	15	2	15	2	16	4	18	2	22	4	18	3	16	2	17	3
Sulfate	10	3	16	4	12	2	11	3	15	4	15	3	12	3	13	2	12	2	12	3
Hematite	4	2	2	2	1	1	1	1	1	1	2	1	3	2	2	1	22	3	2	1
Carbonate	3	1	2	1	4	1	3	1	3	1	3	1	3	1	3	1	2	1	4	1
Quartz	0	0	0	0	0	0	1	0	1	0	1	0	0	0	1	0	0	0	1	0

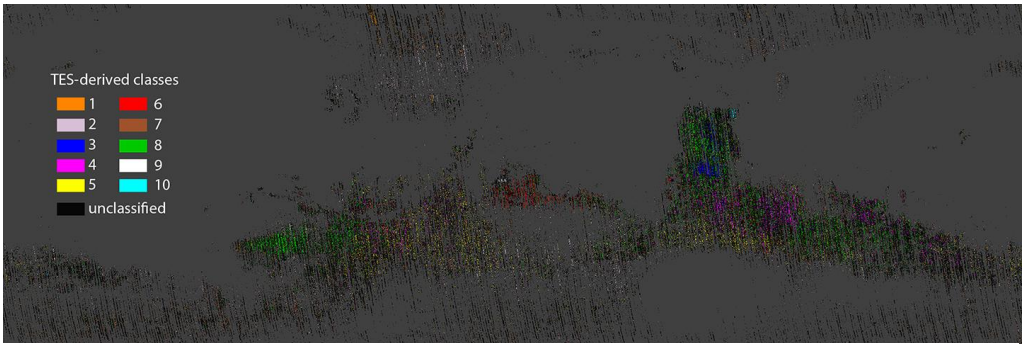

Fig. 4. TES-derived compositional classes from combined IC analysis and supervised classification.

References: [1] Bandfield, *JGR, 107, E6*, 5042 (2002); [2] Poulet et al., *JGR, E08S02* (2007); [3] Boynton et al., *JGR, E12S99* (2007); [4] Rogers and Christensen, *JGR, E01003* (2007); [5] Koeppen and Hamilton, *JGR, 113, E05001* (2008); [6] Karunatillake et al., *JGR 114, E12001* (2009); [7] Gasnault et al., *Icarus, 207* (2010); [8] Taylor et al., *Geology 38*, 2010; [9] Ody et al., *JGR 117*, E00J14 (2012) [10] Ramsey and Christensen, *JGR 103, 557-576* (1998) [11] Hyvarinen and Oja, *Neur. Networks*, 113, 411-430 (2000) [12] Andrews-Hanna et al., *JGR, 115, E06002* (2010) [13] Clenet et al., JGR, 118, 1632-1655 (2013) [14] Kraft et al., *41st LPSC, Abs. #2600* (2010).